Plasmon-polaritonic quadrupole topological insulators

Ying Chen,[1] Zhi-Kang Lin,[2] Huanyang Chen,[1,*] and Jian-Hua Jiang [2,†]

[1]*Institute of Electromagnetics and Acoustics and Key Laboratory of Electromagnetic Wave Science and Detection Technology, Xiamen University, Xiamen 361005, China*
[2]*School of Physical Science and Technology, and Collaborative Innovation Center of Suzhou Nano Science and Technology, Soochow University, 1 Shizi Street, Suzhou, 215006, China*

Quadrupole topological insulator is a symmetry-protected higher-order topological phase with the intriguing topology of Wannier bands, which, however, has not yet been realized in plasmonic metamaterials. Here, we propose a lattice of plasmon-polaritonic nanocavities which can realize quadrupole topological insulators by exploiting the geometry-dependent sign reversal of the couplings between the daisylike nanocavities. The designed system exhibits various topological and trivial phases as characterized by the nested Wannier bands and the topological quadrupole moment which can be controlled by the distances between the nanocavities. Our study opens a pathway toward plasmonic topological metamaterials with quadrupole topology.

I. INTRODUCTION

Higher-order topological insulators (HOTIs) [1–26] provide a new platform for the study of topological photonics, an emergent branch of science in search of topological phenomena and their applications in photonics [27–45]. HOTIs support multidimensional topological boundary states in a single physical system [11,18,26], e.g., the edge and corner states in two-dimensional photonic HOTIs, which can be exploited as topological waveguides and cavity modes in integrated photonic chips. A prototype of HOTIs is the quadrupole topological insulator (QTI), which exhibits gapped edge states and in-gap corner states [1,2,7–9]. The QTIs are fundamentally different from conventional topological insulators [27,28] due to their quantized quadrupole moment and the topology of Wannier bands. The Benalcazar-Bernevig-Hughes (BBH) model is the first theoretical model [1,2] for the QTIs, which is recently realized in mechanical metamaterials [7], electric circuits [8,9], and coupled-ring resonators [17].

On the other hand, plasmon-polaritonic systems offer versatile and effective ways to guide light and to control various photonic modes and their couplings. Plasmonics provides important applications in a broad range of disciplines in photonics with the concepts of plasmonic metamaterials and plasmonic nanophotonics [46–48]. Recently, plasmonic metamaterials have been shown to host conventional topological insulator phases of photons [49–52]. However, higher-order topological phases of photons in plasmonic systems are yet to be studied.

In this paper, we propose a scheme toward plasmon-polaritonic QTIs. By utilizing the geometry-dependent sign reversal of the couplings between daisylike plasmonic modes, we are able to realize the BBH model for the QTIs in

plasmonic systems. Various topological and trivial phases can be realized by tuning the distances between the daisylike cavities, exhibiting versatile topological phenomena related to Wannier bands and topological edge polarizations. Our study opens a pathway toward higher-order quadrupole topological phenomena in plasmonic metamaterials.

II. RESULTS

The designed photonic systems consist of a square lattice of daisylike cavities embedded into a metallic background as illustrated in Fig. 1(a). The unit cell consists of two six-petaled cavities filled with air and two eight-petaled cavities filled with a dielectric material of permittivity $\varepsilon_2 = 1.525$. The lattice constant a is fixed as 1050 nm in our model. The structure of the unit cell is shown in Fig. 1(b). The daisylike geometry can be described analytically in polar coordinates. Explicitly, $r_1(\theta) = r_{01} + d_1\cos(6\theta)$ for the six-petaled cavity, while $r_2(\theta) = r_{02} + d_2\cos(8\theta)$ for the eight-petaled cavity. We adopt $r_{01} = 0.17a$, $d_1 = 0.062a$, $r_{02} = 0.155a$, and $d_2 = 0.095a$. The dashed circles in Fig. 1(a) thus have the inner and outer radii of $r_{01} - d_1$ and $r_{01} + d_1$ ($r_{02} - d_2$ and $r_{02} + d_2$) for the six-petaled (eight-petaled) cavity, respectively. The above material and geometry parameters are designed to ensure the frequency resonance between the hexagonal mode in the six-petaled cavity and the octopolar mode in the eight-petaled cavity [53]. The electric-field profiles for these modes are shown in Fig. 1(a). The permittivity of the metallic background is modeled by a Drude-like form to induce the plasmon polaritons, $\varepsilon_b = 1 - \omega_p^2/(\omega^2 + i\gamma\omega)$. For the calculations in this work, we adopt $\omega_p = 1.37 \times 10^{16}$ s^{-1} (close to silver's plasmon frequency) [54], although our theory can be applied to other plasmonic systems. For the sake of simplicity, the Drude loss γ which induces the dissipation and non-Hermitian effects, is ignored in the main text. However, we discuss the effect of Drude loss in Supplemental Material [53]. We notice that the non-Hermitian

*kenyon@xmu.edu.cn
†jianhuajiang@suda.edu.cn
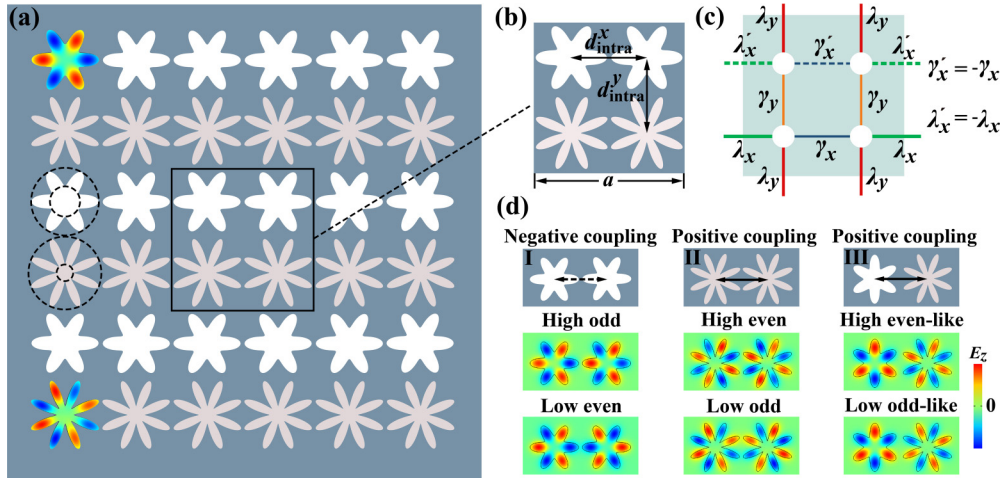
FIG. 1. (a) Structure of the designed plasmon-polaritonic system that realizes the BBH tight-binding model for the QTI [illustrated in right panel (c)]. The square-lattice system consists of two types of daisylike cavities: the six-petaled and the eight-petaled cavities. Left-up (left-down) corner: the electric-field profile for the hexagonal (octupole) resonance in the six-petaled (eight-petaled) cavities. (b) The unit-cell structure with lattice constant $a = 1050$ nm. The tunable geometry parameters are the intra-unit-cell distances, d_{intra}^x and d_{intra}^y, along the x and y directions, respectively. (c) The BBH tight-binding model for the QTI. The unit cell is illustrated by the gray region. (d) Illustration of the pole-pole orientation (negative coupling) or node-node orientations (positive coupling).

effect in higher-order topological insulators is also studied in Ref. [55].

The focus of this work is to show that the BBH model of QTIs [illustrated in Fig. 1(b)] can be realized in plasmon-polaritonic lattice systems by exploiting the geometry-dependent sign reversal of couplings between the daisylike cavities. Such tunable tight-binding couplings between the cavities rely essentially on the evanescent-wave nature of the plamon polaritons. We emphasize that due to the localization of the cavity modes, the next-nearest-neighbor couplings are negligible in the plasmon-polaritonic systems deisgned in this work. We show that within the nearest-neighbor tight-binding approximation, the plasmon-polaritonic systems proposed here can realize the BBH tight-binding model and the QTI phase.

To realize the BBH model, it is important to achieve the tight-binding configuration in Fig. 1(c). The main challenge is to realize simultaneously both the negative and positive couplings. We now show that the sign of the coupling between the daisylike cavities can be well controlled by their orientations. Computationally, such a coupling can be determined by half of the difference between the frequencies of the even (ω_e) and the odd (ω_o) hybridized modes of the two coupled cavities, i.e., $t = \frac{1}{2}(\omega_e - \omega_o)$. For instance, as shown in Fig. 1(d), the coupling along the x direction between the six-petaled cavities is negative, since the the odd mode has higher frequency than the even mode. It turns out that the coupling along the y direction between the six-petaled cavities has the opposite sign, i.e., the coupling is positive. This sign reversal for couplings between the plasmon-polaritonic cavity modes is an intriguing phenomenon discovered in Ref. [56]. In fact, the sign of the coupling depends on whether it is a pole-pole orientation (negative coupling) or node-node orientation (positive coupling) for the two coupled cavities [see Fig. 1(d)]. Exploiting such a mechanism, the BBH model can be realized

within the nearest-neighbor tight-binding approximation in the plasmon-polaritonic systems studied in this work.

We find from first-principle calculations that the coupling strengths between the nearest-neighbor cavities have exponential dependences on the center-to-center distance between them [53]. Such exponential dependences are signatures of evanescent wave couplings which justify the tight-binding approximation. On the other hand, such dependences enable control of the relative strength between the intra-unit-cell couplings (γ_x and γ_y) and the inter-unit-cell couplings (λ_x and λ_y) through the intra-unit-cell distances (d_{intra}^x and d_{intra}^y) and the inter-unit-cell distances ($d_{\text{inter}}^x = a - d_{\text{intra}}^x$ and $d_{\text{inter}}^y = a - d_{\text{intra}}^y$). Figure 2(a) presents the evolution of the tight-binding coefficients with the ratio $d_{\text{intra}}/d_{\text{inter}}$ when $d_{\text{intra}}^x = d_{\text{intra}}^y \equiv d_{\text{intra}}$ with $d_{\text{inter}} = a - d_{\text{intra}}$. The figure shows that the tight-binding coefficients can be effectively controlled by the geometry parameters. In particular, the sign reversal of the couplings $\gamma_x' = -\gamma_x$ and $\lambda_x' = -\lambda_x$ holds for all geometry parameters. With such geometric control, the relative strength of the intra-unit-cell coupling and the inter-unit-cell coupling can be switched. By mapping the plasmon-polaritonic system into the BBH tight-binding model within the nearest-neighbor approximation, we can determine the topological phase diagram of the plasmon-polaritonic systems using the phase diagram of the BBH model in Refs. [2,12].

As shown in Fig. 2(b), the topological transitions in our plasmon-polaritonic system take place at the two lines $d_{\text{intra}}^x = d_{\text{inter}}^x$ and $d_{\text{intra}}^y = d_{\text{inter}}^y$. Four different phases are separated by the two lines as shown in Fig. 2(b). Those phases are characterized by their topological edge polarizations $\vec{p}^E = (p_x^{E_y}, p_y^{E_x})$, where $p_y^{E_x}$ ($p_x^{E_y}$) represents the polarization along the y (x) direction for the edges normal to the x (y) direction. The QTI has $\vec{p}^E = (\frac{1}{2}, \frac{1}{2})$, while the trivial phase without edge or corner state has $\vec{p}^E = (0, 0)$. There are two other first-order weak topological insulators with $\vec{p}^E = (\frac{1}{2}, 0)$ and
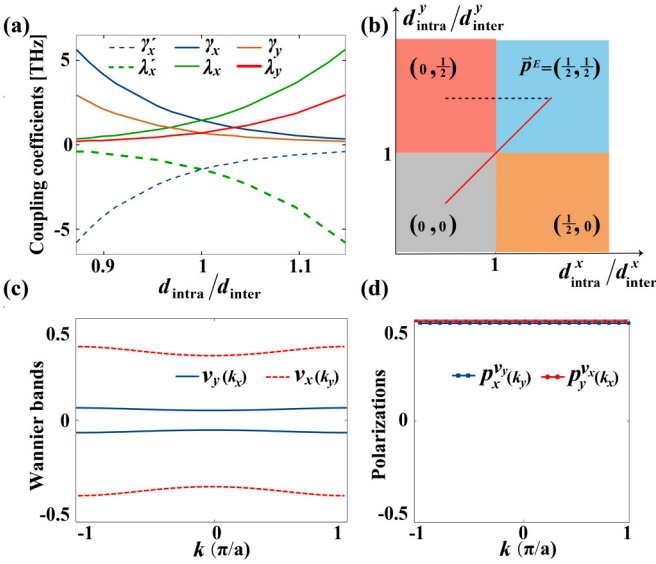
FIG. 2. (a) Dependences of the tight-binding coefficients on the ratio d_{intra}/d_{inter}, when $d_{intra}^x = d_{intra}^y \equiv d_{intra}$ with $d_{inter} \equiv a - d_{intra}$. (b) Topological phase diagram for the plasmon-polaritonic system. (c) The Wannier bands and (d) nested Wannier bands for the case with $d_{intra}/d_{inter} = 1.15$.

$\vec{p}^E = (0, \frac{1}{2})$, respectively. They have edge states only along the x or the y direction, respectively. The quadrupole topological index is related to the bulk-induced edge polarization as $q_{xy} = 2p_x^{E_y} p_y^{E_x}$. Therefore, q_{xy} is nontrivial only in the $\vec{p}^E = (\frac{1}{2}, \frac{1}{2})$ phase.

To characterize the quadrupole topology from the Berry phases, we calculate the Wannier bands and the nested Wannier bands [1,2]. The Wannier bands are defined through the Wilson-loop operators as follows. The Wilson-loop operator along the y direction is $\hat{W}_{y,\mathbf{k}}(k_x) = \mathcal{T}_P \exp[i \oint \hat{A}^y(\mathbf{k}) dk_y]$, where the subscripts y and $\mathbf{k}$ denote the direction and the starting point of the loop, respectively. $\hat{A}^y(\mathbf{k})$ is the Berry connection matrix where $A_{nm}^y(\mathbf{k}) = i\langle u_m(\mathbf{k})|\partial_{k_y}|u_n(\mathbf{k})\rangle$ with $|u_n(\mathbf{k})\rangle$ being the periodic part of the Bloch wave function for the nth band with the wave vector $\mathbf{k}$. Here, $\mathcal{T}_P$ represents the path-ordering operator along a closed loop in the Brillouin zone.

In the BBH model, there are four bands where two of them are below the topological band gap. When these two bands are included in the Wilson-loop calculation (i.e., $n, m = 1, 2$), the Wilson-loop operator becomes a 2×2 matrix. The Wilson-loop operator essentially calibrates the polarization along the y direction. Thus, the eigenvalues of the Wilson-loop operator are the Wannier centers along the y direction, which are obtained by diagonalizing the Wilson-loop operator matrix, $\hat{W}_{y,\mathbf{k}} \boldsymbol{\eta}_{y,\mathbf{k}}^j = e^{2\pi i \nu_y^j(k_x)} \boldsymbol{\eta}_{y,\mathbf{k}}^j$. Here, $\boldsymbol{\eta}_{y,\mathbf{k}}^j$ is the eigenvector for the jth Wannier band ($j = 1, 2$). The jth Wannier band is explicitly the dependence of the Wannier center $\nu_y^j(k_x)$ on the wave vector k_x [see Fig. 2(c)]. The Wannier basis is defined as [1,2] $|w_j(\mathbf{k})\rangle = \sum_{n=1}^2 [\boldsymbol{\eta}_{y,\mathbf{k}}^j]^n |u_n(\mathbf{k})\rangle$. The nested Wannier band is given by the eigenvalues of the nested Wilson loop along the x direction for the Wannier basis $p_x^{\nu_y}(k_y) = \frac{1}{2\pi} \oint \tilde{A}_1^x(\mathbf{k}) dk_x$, with $\tilde{A}_1^x(\mathbf{k}) = i\langle w_1(\mathbf{k})|\partial_{k_x}|w_1(\mathbf{k})\rangle$ being the Berry connection for the first Wannier band. Similarly, one can calculate the

Wannier bands and nested Wannier bands for the Wilson loop along the x direction and the nested Wilson loop along the y direction.

The QTIs are featured with two fundamental characteristics: First, the Wannier bands are gapped (meaning that ν_y and ν_x must not be 0 or $\frac{1}{2}$) and symmetric around 0. Such Wannier bands imply that the total bulk dipole polarization vanishes for the topological band, which is a unique feature of QTIs that distinguishes itself from many other higher-order topological insulators [1,2]. Second, the Wannier-sector polarizations must be nontrivial, $p_x^{\nu_y} = p_y^{\nu_x} = \frac{1}{2}$, where $p_x^{\nu_y}$ is the average of the nested Wannier bands, i.e., $p_x^{\nu_y} = \frac{a}{2\pi} \int dk_y p_x^{\nu_y}(k_y)$ and $p_y^{\nu_x} = \frac{a}{2\pi} \int dk_x p_y^{\nu_x}(k_x)$. It has been demonstrated in Ref. [2] that the Wannier-sector polarizations are equal to the topological edge polarizations induced by the bulk Bloch bands, i.e., $p_x^{E_y} = p_x^{\nu_y}$ and $p_y^{E_x} = p_y^{\nu_x}$. As shown in Figs. 2(c) and 2(d), the calculated Wannier bands are indeed gapped and the nested Wannier bands are indeed nontrivially quantized to $\frac{1}{2}$ for the QTI phase.

To reveal the nature of the topological phase transitions in the plasmon-polaritonic systems, we study the evolution of the Wannier bands, Wannier-sector polarizations, and the spectrum for a finite-sized (8×8 unit cells) supercell from both the tight-binding calculation and the electromagnetic-wave simulation. We first study the evolution of those quantities along the red line in the phase diagram Fig. 2(b), where $d_{intra}^x = d_{intra}^y \equiv d_{intra}$ and $d_{inter} \equiv a - d_{intra}$. The topological transition takes place at $d_{intra} = d_{inter} = a/2$ where the bulk band gap closes. We emphasize that for the Wannier-sector polarizations to be well defined, both the bulk band gap and the Wannier gap are needed. We thus avoid the calculation of the Wannier bands in the vicinity of the phase-transition point in Figs. 3(a) and 3(b). In addition, our model is intrinsically anisotropic: even when $d_{intra}^x = d_{intra}^y$, the strengths of the tight-binding couplings along the x and y directions are different. Therefore, the Wannier bands, $\nu_y(k_x)$ and $\nu_x(k_y)$, are different, as shown in Figs. 3(a) and 3(b) [also in Fig. 2(c)]. Across the topological transition, the Wannier-sector polarizations, $p_x^{\nu_y}$ and $p_y^{\nu_x}$, change from 0 to $\frac{1}{2}$. This is a transition from the trivial phase to the QTI phase, which is consistent with the phase diagram in Fig. 2(b).

The evolution of the spectrum for the supercell with 8×8 unit cells is shown in Figs. 3(c) and 3(d). The former is from the tight-binding calculation, while the latter is from the electromagnetic-wave simulation. The results from these two approaches agree well with each other, confirming the validity of the tight-binding approximation. Here, the spectra include the bulk, edge, and corner states. With increasing d_{intra}/d_{inter}, the bulk band gap closes and reopens to enter into the QTI phase. The corner states emerge immediately when the topological bulk gap opens, demonstrating directly the higher-order bulk-corner correspondence.

We then study the topological transition along the black line in the phase diagram [Fig. 2(b)] where d_{intra}^x is changed but with d_{intra}^y fixed. With increasing d_{intra}^x, the Wannier band ν_y experiences gap closing (i.e., ν_y goes to 0.5) and reopening [see Fig. 3(e)], while the Wannier band ν_x is kept as gapped [Fig. 3(f)]. Accompanying this transition, the Wannier-sector polarization goes from $p_x^{\nu_y} = 0$ to $p_x^{\nu_y} = \frac{1}{2}$, while the $p_y^{\nu_x}$ is
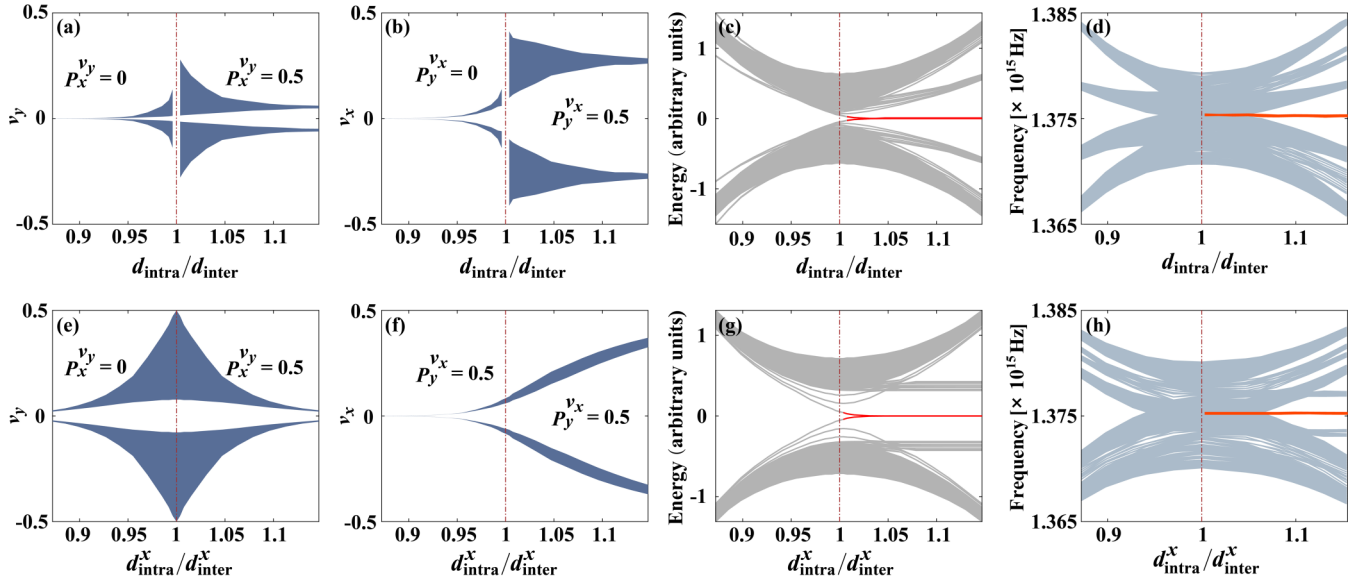
FIG. 3. (a), (b) Evolution of the Wannier bands, ν_y and ν_x, along the red line in the phase diagram [Fig. 2(b)] where $d_{intra}^x = d_{intra}^y \equiv d_{intra}$ and $d_{inter} \equiv a - d_{intra}$. (c), (d) Evolution of the spectra for a finite-sized supercell with 8×8 unit cells from (c) tight-binding calculation and (d) electrodynamic simulation. (e), (f) Evolution of the Wannier bands, ν_y and ν_x, along the black line in the phase diagram [Fig. 2(b)] where d_{intra}^x is changed but d_{intra}^y is fixed. (g), (h) Evolution of the spectra in a finite-sized supercell with 8×8 unit cells from (c) tight-binding calculation and (d) electrodynamic simulation. The red lines in those figures indicate the corner states in the QTI phase.

kept as $\frac{1}{2}$. For the spectrum of the finite-sized supercell, both the tight-binding calculation and the electromagnetic-wave simulation give the same feature that the corner states emerge after the transition, which confirms the topological phase diagram.

We now show explicitly the emergence of the corner states in the designed plasmon-polaritonic system. Figure 4(a) presents the spectrum of the supercell with 8×8 unit cells

for $d_{intra}/d_{inter} = 1.15$ which is in the QTI phase. Four corner states emerge in the bulk band gap. In contrast, for the trivial phase with $d_{intra}/d_{inter} = 0.87$, there are no corner states in the bulk band gap [see Fig. 4(b)]. The electric-field profiles of the four corner states for the QTI phase are presented in Fig. 4(c). These results demonstrate convincingly the connection between the quadrupole topology and the in-gap corner states. The edge states for the QTI phase as
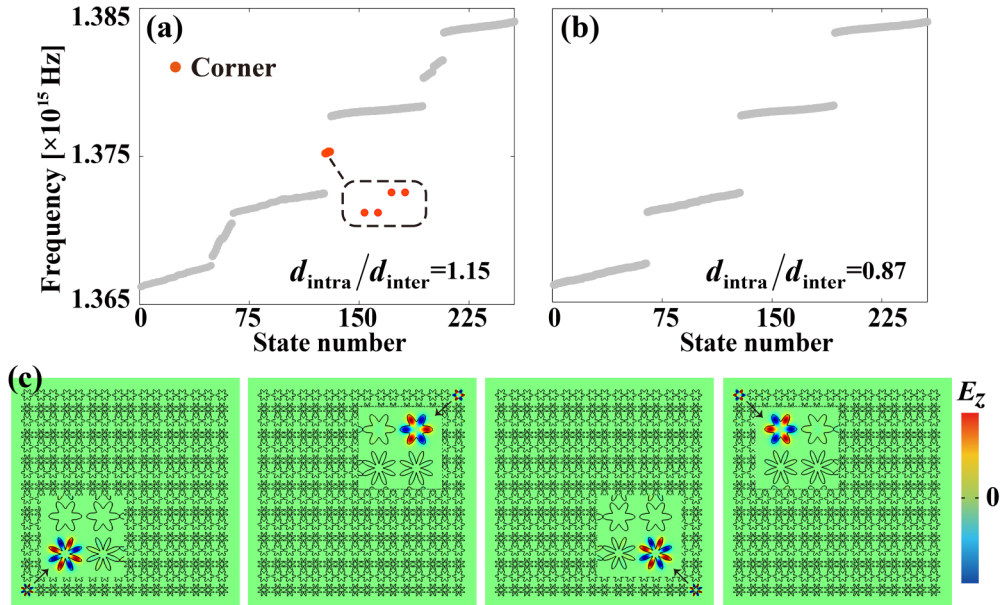
FIG. 4. (a) Spectrum of the supercell with 8×8 unit cells for $d_{intra}/d_{inter} = 1.15$ from electromagnetic-wave simulation. The horizontal axis is the number of the eigenmode solution labeled with ascending frequency order. (b) The spectrum for similar supercell but with $d_{intra}/d_{inter} = 0.87$. (c) Distributions of the electric field along the z direction, E_z, for the four corner states in (a). Insets are the zoom-in of the electric-field profiles for the corner states.

well as those for the weak topological phases are shown in Ref. [53].

Finally, we remark that, since for the finite-sized structures, the mirror symmetry along the y direction, i.e., $M_y : y \rightarrow -y$, is broken, the four corner states in Fig. 4(a) are not degenerate, but split into two pairs. One pair of corner states are localized at the upper boundary, while the other pair of corner states are localized at the lower boundary.

III. CONCLUSIONS AND OUTLOOK

We propose a scheme to realize QTIs in plasmon-polaritonic systems. The key ingredient is the sign-reversal mechanism for the couplings between the plasmon-polaritonic cavities from the pole-pole orientation to the node-node orientation. The designed plasmon-polaritonic system demonstrates various topological and trivial phases which can be controlled by the distances between the cavities. Our study introduces quadrupole topology and its topological transitions into plasmonic metamaterials which may inspire future studies on topological metamaterials and their potential applications.

[1] W. A. Benalcazar, B. A. Bernevig, and T. L. Hughes, Science **357**, 61 (2017).

[2] W. A. Benalcazar, B. A. Bernevig, and T. L. Hughes, Phys. Rev. B **96**, 245115 (2017).

[3] J. Langbehn, Y. Peng, L. Trifunovic, F. von Oppen, and P. W. Brouwer, Phys. Rev. Lett. **119**, 246401 (2017).

[4] Z. D. Song, Z. Fang, and C. Fang, Phys. Rev. Lett. **119**, 246402 (2017).

[5] R. J. Slager, L. Rademaker, J. Zaanen, and L. Balents, Phys. Rev. B **92**, 085126 (2015).

[6] M. Ezawa, Phys. Rev. Lett. **120**, 026801 (2018).

[7] M. Serra-Garcia, V. Peri, R. Süsstrunk, O. R. Bilal, T. Larsen, L. G. Villanueva, and S. D. Huber, Nature (London) **555**, 342 (2018).

[8] C. W. Peterson, W. A. Benalcazar, T. L. Hughes, and G. Bahl, Nature (London **555**, 346 (2018).

[9] S. Imhof, C. Berger, F. Bayer, J. Brehm, L. W. Molenkamp, T. Kiessling, F. Schindler, C. H. Lee, M. Greiter, T. Neupert, and R. Thomale, Nat. Phys. **14**, 925 (2018).

[10] J. Noh, W. A. Benalcazar, S. Huang, M. J. Collins, K. P. Chen, T. L. Hughes, and M. C. Rechtsman, Nat. Photonics **12**, 408 (2018).

[11] F. Schindler, A. M. Cook, M. G. Vergniory, Z. J. Wang, S. S. P. Parkin, B. A. Bernevig, and T. Neupert, Sci. Adv. **4**, eaat0346 (2018).

[12] W. A. Wheeler, L. K. Wagner, and T. L. Hughes, Phys. Rev. B **100**, 245135 (2019).

[13] B. Y. Xie, H. F. Wang, H. X. Wang, X. Y. Zhu, J. H. Jiang, M. H. Lu, and Y. F. Chen, Phys. Rev. B **98**, 205147 (2018).

[14] H. R. Xue, Y. H. Yang, F. Gao, Y. D. Chong, and B. L. Zhang, Nat. Mater. **18**, 108 (2019).

[15] X. Ni, M. Weiner, A. Alu, and A. B. Khanikaev, Nat. Mater. **18**, 113 (2019).

[16] X. Zhang, H. X. Wang, Z. K. Lin, Y. Tian, B. Xie, M. H. Lu, Y.-F. Chen, and J.-H. Jiang, Nat. Phys. **15**, 582 (2019).

[17] S. Mittal, V. V. Orre, G. Y. Zhu, M. A. Gorlach, A. Poddubny, and M. Hafezi, Nat. Photonics **13**, 692 (2019).

[18] A. E. Hassan, F. K. Kunst, A. Moritz, G. Andler, E. J. Bergholtz, and M. Bourennane, Nat. Photonics **13**, 697 (2019).

[19] H. Y. Fan, B. Xia, L. Tong, S. Zheng, and D. J. Yu, Phys. Rev. Lett. **122**, 204301 (2019).

[20] Y. Ota, F. Liu, R. Katsumi, K. Watanabe, K. Wakabayashi, Y. Arakawa, and S. Iwamoto, Optica **6**, 786 (2019).

[21] X. D. Chen, W. M. Deng, F. L. Shi, F. L. Zhao, M. Chen, and J. W. Dong, Phys. Rev. Lett. **122**, 233902 (2019).

[22] B. Y. Xie, G. X. Su, H. F. Wang, H. Su, X. P. Shen, P. Zhan, M. H. Lu, Z. L. Wang, and Y. F. Chen, Phys. Rev. Lett. **122**, 233903 (2019).

[23] L. Zhang, Y. Yang, P. Qin, Q. Chen, F. Gao, E. Li, J.-H. Jiang, B. Zhang, and H. Chen, arXiv:1901.07154 (2019).

[24] Y. Chen, X. C. Lu, and H. Y. Chen, Opt. Lett. **44**, 4251 (2019).

[25] Z. K. Lin, H. X. Wang, M. H. Lu, and J. H. Jiang, arXiv:1903.05997 (2019).

[26] B. Kang, K. Shiozaki, and G. Y. Cho, Phys. Rev. B **100**, 245134 (2019).

[27] M. Z. Hasan and C. L. Kane, Rev. Mod. Phys. **82**, 3045 (2010).

[28] X. L. Qi and S. C. Zhang, Rev. Mod. Phys. **83**, 1057 (2011).

[29] Z. Wang, Y. Chong, J. D. Joannopoulos, and M. Soljacic, Nature (London) **461**, 772 (2009).

[30] M. Hafezi, E. A. Demler, M. D. Lukin, and J. M. Taylor, Nat. Phys. **7**, 907 (2011).

[31] Y. Poo, R.-x. Wu, Z. Lin, Y. Yang, and C. T. Chan, Phys. Rev. Lett. **106**, 093903 (2011).

[32] Y. E. Kraus, Y. Lahini, Z. Ringel, M. Verbin, and O. Zilberberg, Phys. Rev. Lett. **109**, 106402 (2012).

[33] M. Hafezi, S. Mittal, J. Fan, A. Migdall, and J. M. Taylor, Nat. Photonics **7**, 1001 (2013).

[34] A. B. Khanikaev, S. H. Mousavi, W. K. Tse, M. Kargarian, A. H. MacDonald, and G. Shvets, Nat. Mater. **12**, 233 (2013).

[35] M. C. Rechtsman, J. M. Zeuner, Y. Plotnik, Y. Lumer, D. Podolsky, F. Dreisow, S. Nolte, M. Segev, and A. Szameit, Nature (London) **496**, 196 (2013).

[36] W. J. Chen, S. J. Jiang, X. D. Chen, B. C. Zhu, L. Zhou, J. W. Dong, and C. T. Chan, Nat. Commun. **5**, 5782 (2014).

[37] L. Lu, J. D. Joannopoulos, and M. Soljacic, Nat. Photonics **8**, 821 (2014).

[38] X. J. Cheng, C. Jouvaud, X. Ni, S. H. Mousavi, A. Z. Genack, and A. B. Khanikaev, Nat. Mater. **15**, 542 (2016).

[39] L. H. Wu and X. Hu, Phys. Rev. Lett **114**, 223901 (2015).

[40] L. Xu, H. X. Wang, Y. D. Xu, H. Y. Chen, and J. H. Jiang, Opt. Express **24**, 18059 (2016).

[41] A. B. Khanikaev and G. Shvets, Nat. Photonics **11**, 763 (2017).

[42] H.-X. Wang, Y. Chen, Z. H. Hang, H.-Y. Kee, and J.-H. Jiang, npj Quantum Mater. **2**, 54 (2017).

[43] X. Zhu, H.-X. Wang, C. Xu, Y. Lai, J.-H. Jiang, and S. John, Phys. Rev. B **97**, 085148 (2018).

[44] Y. Chen, L. Xu, G. X. Cai, and H. Y. Chen, Phys. Rev. B **98**, 125430 (2018).

[45] T. Ozawa, H. M. Price, A. Amo, N. Goldman, M. Hafezi, L. Lu, M. C. Rechtsman, D. Schuster, J. Simon, O. Zilberberg, and I. Carusotto, Rev. Mod. Phys. **91**, 015006 (2019).

[46] S. A. Maier, *Plasmonics: Fundamentals and Applications* (Springer, New York, 2007).

[47] A. Boltasseva and H. A. Atwater, Science **331**, 290 (2011).

[48] K. Yao and Y. M. Liu, Nanotechnol. Rev. **3**, 177 (2014).

[49] F. Gao, Z. Gao, X. H. Shi, Z. J. Yang, X. Lin, H. Y. Xu, J. D. Joannopoulos, M. Soljacic, H. S. Chen, L. Lu, Y. D. Chong, and B. L. Zhang, Nat. Commun. **7**, 11619 (2016).

[50] S. Yves, R. Fleury, T. Berthelot, M. Fink, F. Lemoult, and G. Lerosey, Nat. Commun. **8**, 16023 (2017).

[51] X. X. Wu, Y. Meng, J. X. Tian, Y. Z. Huang, H. Xiang, D. Z. Han, and W. J. Wen, Nat. Commun. **8**, 1304 (2017).

[52] Z. Gao, L. Wu, F. Gao, Y. Luo, and B. L. Zhang, Adv. Mater. **30**, 1706683 (2018).

[53] See Supplemental Material at http://link.aps.org/supplemental/10.1103/PhysRevB.101.041109 for the details of the cavity modes, the effect of Drude loss, the couplings between the cavity modes, and the edge states for the quadrupole and weak topological phases.

[54] M. A. Ordal, L. L. Long, R. J. Bell, S. E. Bell, R. R. Bell, R. W. Alexander, and C. A. Ward, Appl. Opt. **22**, 1099 (1983).

[55] T. Liu, Y. R. Zhang, Q. Ai, Z. P. Gong, K. Kawabata, M. Ueda, and F. Nori, Phys. Rev. Lett. **122**, 076801 (2019).

[56] Z. Gao, F. Gao, Y. M. Zhang, H. Y. Xu, Y. Luo, and B. L. Zhang, Adv. Mater. **29**, 1700018 (2017).